Impact of Thermoelectric Effects on Phase Change Memory Characteristics

Nicola Ciocchini, *Student Member, IEEE*, Mario Laudato, *Student Member, IEEE*, Antonio Leone, Paolo Fantini, Andrea L. Lacaita, *Fellow, IEEE*, and Daniele Ielmini, *Senior Member, IEEE*

I. Introduction

PHASE change memory (PCM) is a nonvolatile memory based on the ability of a chalcogenide alloy to reversibly switch from a crystalline phase with low electrical resistance (few kiloohms) to an amorphous phase with high electrical resistance (few megaohms) [1]. Switching between the two phases is obtained by the application of voltage pulses, inducing Joule heating in the phase change chalcogenide material. PCM was demonstrated to have excellent scalability [2], fast switching [3], and long data retention [4]. The possibility to tune the device property by changing the composition of the phase change material makes PCM suitable for a large range of applications, from standalone to embedded memory [5]. To better assess the potential of PCM in memory and storage applications, the
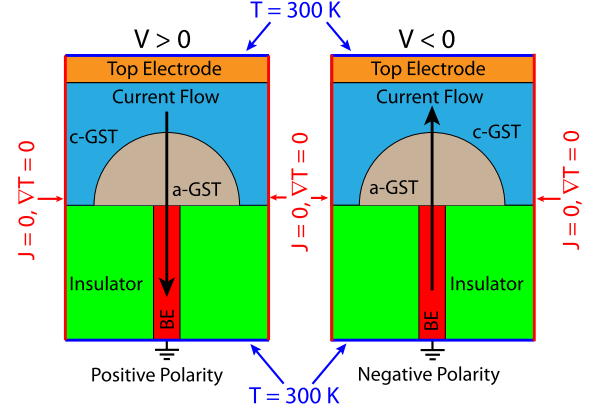

Fig. 1. Schematic of the PCM used in our experiments, with GST film enclosed between a top electrode and a confined BE. The two sketches indicate operation under a positive (left) or negative (right) voltage applied to the top electrode. The boundary conditions of the finite-element model in Section VI are also indicated.

N. Ciocchini, M. Laudato, A. Leone, A. L. Lacaita, and D. Ielmini are with the Italian Universities Nanoelectronics Team, Dipartimento di Elettronica, Informazione e Bioingegneria, Politecnico di Milano, Milan 20133, Italy (e-mail: nicola.ciocchini@polimi.it; mario.laudato@polimi.it; antonio.leone@polimi.it; andrea.lacaita@polimi.it; daniele.ielmini@polimi.it).

P. Fantini is with the Research and Development Process, Micron Semiconductor Italia srl via Torri Bianche, 24 20871 Vimercate, Italy (e-mail: pfantini@micron.com).

Color versions of one or more of the figures in this paper are available online.
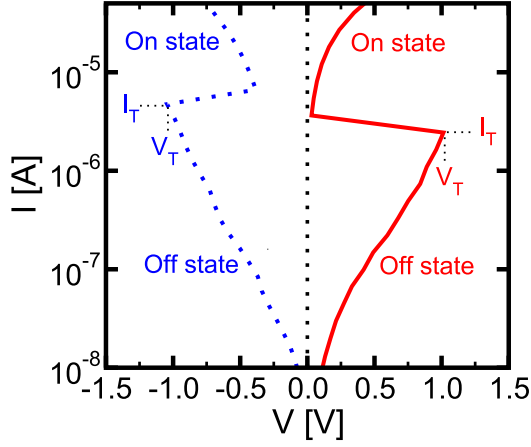
thermal/electrical phenomena controlling heating and phase transition must be carefully understood and modeled.

In this paper, we address the impact of thermoelectric (TE) in PCM devices from both experimental and modeling points of view. Our experimental results show that a different heating takes place under negative and positive voltage polarities, which is attributed to TE. The experimental findings are summarized on a universal plot relating the positive and negative voltage for major thermally induced phenomena in the PCM, namely, melting, crystallization, holding of the ON-state, and ion migration in both the ON- and OFF-states. We refine our finite-element model of the PCM [6] to describe Joule heating combined with Thomson, Peltier, and Seebeck effects. The model correctly accounts for the universal TE characteristic, highlighting the relevance of TE to achieve energy-efficient PCM devices. The model is finally used to evaluate the impact of isotropic scaling on TE.

II. Set Regime

We performed experiments on mushroom-type PCM cells in 45-nm technology [7], with $Ge_2Sb_2Te_5$ (GST) as active material. Fig. 1 schematically shows the PCM device in the mushroom structure. The GST layer is enclosed between a top electrode and a confined bottom electrode (BE) contact, which allows for efficient Joule heating inside the phase change layer. Fig. 1 also shows the voltage sign convention adopted in this paper, where the BE is grounded and the

Fig. 2. Measured I–V curves for a PCM device in the reset state at positive and negative voltages. Threshold voltage V_T and threshold current I_T are also shown.
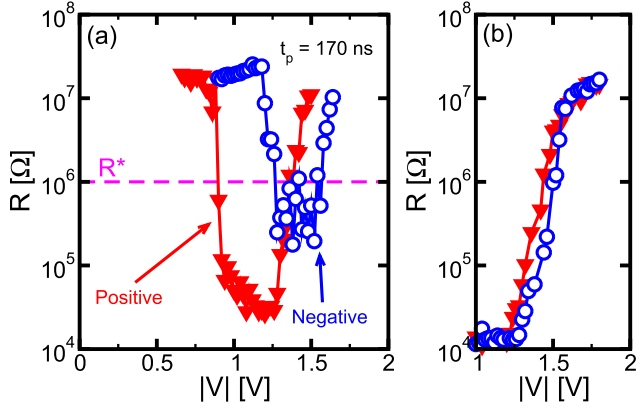

Fig. 3. (a) Measured R as a function of programming voltage V for a reset-state PCM. The characteristics for positive and negative V are compared. Set/reset transitions shift to higher voltages for $V < 0$. (b) Measured R as a function of V for a set-state PCM for positive and negative V. The reset transition takes place at higher V for negative voltage.

Fig. 4. Color map of the measured R as a function of pulse amplitude V and pulse duration t_P for (a) $V < 0$ and (b) $V > 0$. R decreases at increasing V due to crystallization (set), and then increases due to melting/reset. A larger V is needed for set transition at $V < 0$.

voltage sign corresponds to the sign of the voltage at the top electrode.

The PCM device was directly connected to a TTi TGA 12102 arbitrary waveform generator for pulse delivery and to an Agilent B2900 parameter analyzer for resistance reading. The two instruments were decoupled by an 8-nF bypass capacitor connected in series to the waveform generator channel. Fig. 2 shows the current–voltage (I–V) characteristics of a PCM cell in the reset (amorphous) state, obtained by the application of a previous positive voltage pulse. The curves are almost symmetric, showing an exponential increase of current with voltage [8] (Poole–Frenkel regime) toward threshold switching, taking place at threshold voltage V_T and threshold current I_T [9]. Device readout is carried out in the region below I_T (OFF-state), while the region above I_T (ON-state) is exploited for program operation [10]. We performed bipolar R read at $I_{read} = \pm 1$ nA, and we verified that the R measured at positive and negative polarities was the same.

Fig. 3(a) shows the programming curve of the PCM. The resistance R is measured after voltage pulses with amplitude V
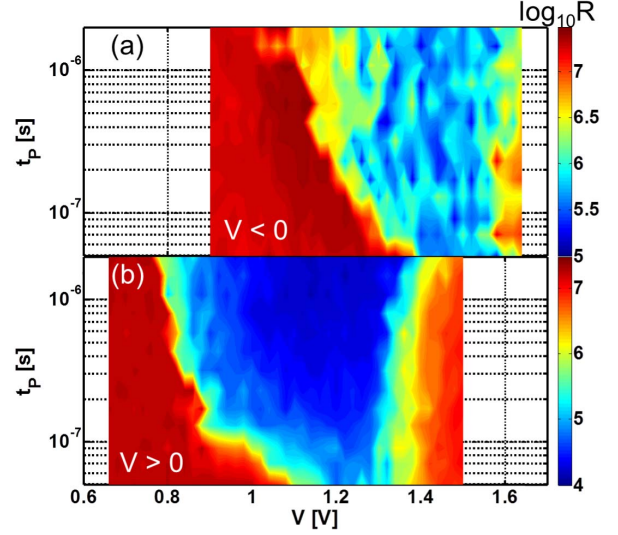
and constant pulsewidth $t_P = 170$ ns. To allow the characterization of programming curve below V_T, the voltage pulse was anticipated by a short pulse ($t_P < 20$ ns) with amplitude above V_T, with negligible impact on GST crystallization [10]. The cell was prepared in the reset state before every programming pulse. As the programming voltage increases, R gradually decreases due to the thermally activated crystallization of the amorphous phase (set transition), and then, R increases as the temperature in the switching layer exceeds the GST melting point $T_m \approx 900$ K [6]. Both effects are thermally driven and are, therefore, expected to be sensitive to TE.

To compare results at different voltage polarities, we defined a set voltage at the crossing of the programming curves with the critical value of resistance $R^* = 1$ MΩ shown in Fig. 3(a). The figure shows that crystallization and melting are shifted to higher voltage for $V < 0$, compared with $V > 0$. We attribute the shift to TE, leading to higher local temperature in the GST volume for $V > 0$ with respect to $V < 0$ at a given $|V|$ [11]. The higher set-state R at $V < 0$ can be attributed to ion migration, consistently with results in Section IV, and to the lower T at $V < 0$ reducing crystallization speed.

Fig. 3(b) shows the R–V characteristics in the reset region for a PCM device initially prepared in the set (crystalline) state. To initialize the device in the set state, a relatively slow voltage sweep was delivered to the cell before every reset pulse. Data confirm the asymmetry in the programming characteristics, where a higher voltage is needed to achieve the melting point and the consequent amorphization at $V < 0$. The smaller shift with respect to Fig. 3(a) can be attributed to the different initial states, i.e., set state instead of reset state, which show different TE parameters.

From results in Figs. 3 and 4, we conclude that electrically induced heating is less efficient for negative bias, which results in a higher voltage needed to trigger crystallization and melting compared with the positive voltage operation. Equivalently, crystallization is slower for $V < 0$ compared
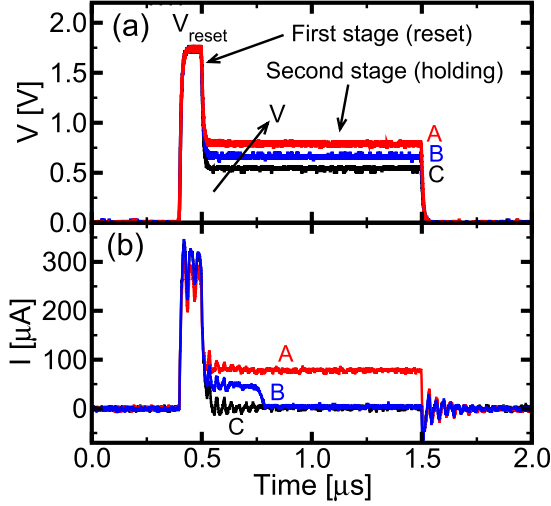
Fig. 5. (a) Applied voltage and (b) measured current to evaluate the holding voltage V_H. The first 100-ns pulse induces reset, and then, the voltage is reduced in the following 1 μs, while the current response is monitored. For $V > V_H$ (A), the ON-state is sustained, while for $V < V_H$ (C), the cell immediately decays to the OFF-state. The condition of unstable ON-state (B) defines $V = V_H$.

with $V > 0$, at a given pulse amplitude $|V|$. Fig. 4 shows programming curves showing R (color map) as a function of V (x-axis) and t_P (y-axis) for negative and positive voltage. Data in the figure confirm that the heating is inhibited for $V < 0$.

III. HOLDING VOLTAGE

To study the impact of TE on electrical transition, we characterized the holding voltage V_H needed to sustain the device in the ON-state in Fig. 2 after threshold switching. Fig. 5 shows the measurement technique to evaluate the holding voltage V_H in our devices. First, a 100-ns reset pulse with amplitude $V_{reset} = 1.75$ V was applied to switch the device in the ON-state [Fig. 5(a)], and then, the voltage was decreased to a lower value V while monitoring the current in real time [Fig. 5(b)]. For $V > V_H$ (A), the cell remains in the ON-state with a current well above 50 μA. For $V < V_H$, instead, the current immediately turns OFF from the ON-state (C). The voltage V_H is defined by the intermediate case (B) where the cell switches OFF in a finite time after the reset pulse.

The waveforms in Fig. 5 allow measuring the I–V curve of the PCM in the ON-state, which is shown in Fig. 6(a). The I–V curve was obtained by taking the average current in the second region of the pulse, as a function of the applied voltage for $V > 0$ and $V < 0$. The sharp drop from the linear ON-state to the high-resistance OFF-state marks the holding voltage V_H. The experimental results clearly indicate a larger V_H at negative voltage, namely, $V_H = 0.74$ V at $V > 0$ and $V_H = -0.92$ V at $V < 0$.

Similar measurements were repeated by changing the amplitude $V_{reset} > 0$ in the first region of the modulated pulse. Fig. 6(b) shows the measured V_H for both positive and negative V, as a function of V_{reset}. The holding voltage increases with V_{reset}, since this defines the thickness of the amorphous volume in which the ON-state must be sustained.
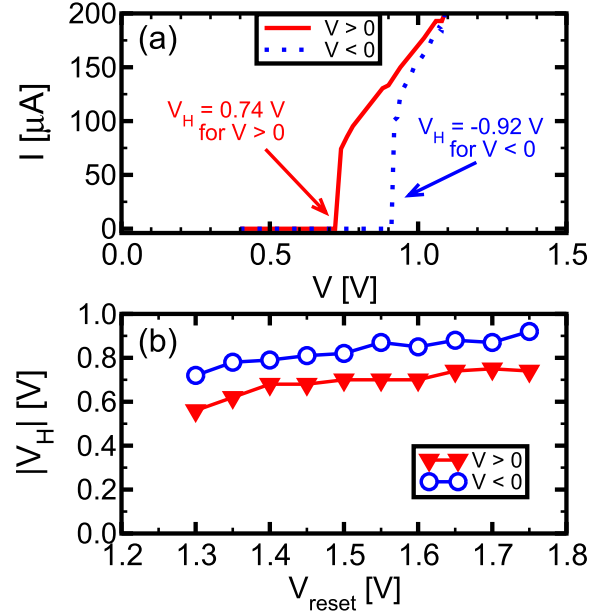

Fig. 6. (a) Measured I–V curves from the technique in Fig. 5 at $V > 0$ and $V < 0$ and (b) measured V_H as a function of the reset pulse voltage V_{reset}. From the I–V curves in (a), one can extract V_H, in correspondence of the sharp drop from the ON-state ($I > 50$ μA) to the OFF-state ($I < 50$ μA). V_H is relatively large for an applied voltage $V < 0$ due to TE causing less efficient heating under negative voltage.

For a larger volume of amorphous GST, a larger voltage is needed to maintain a sufficiently high temperature over the whole amorphous volume. Most importantly, the holding voltage is generally higher at negative voltage compared with $V > 0$, in agreement with the polarity dependence of phase transition voltages in Fig. 3. These experiments suggest that the temperature significantly contributes to the holding process, and thus making it sensitive to polarity-dependent TE.

IV. ION MIGRATION

Previous works addressed ion migration in PCM under relatively high-voltage pulse where a significant fraction of the chalcogenide material is in the liquid phase [12], [13]. However, ion migration induced by the local temperature and electric field might also take place in the solid state, as a result of ionic diffusion and drift of cations/anions in both the crystalline and amorphous phases of GST. To investigate ion migration effects in the solid state, we studied the kinetics of ion migration below melting in both the ON- and the OFF-state.

Regarding the ON-state migration, Fig. 7(a) shows the resistance measured after the application of a negative voltage pulse to a PCM device prepared in the set state, as a function of the pulsewidth t_P. The negative voltage applied to the cell leads to an increase of R, which can be ascribed to the voltage-driven migration of cations (e.g., Sb) and anions (e.g., Te), resulting in the accumulation of Te and the depletion of Sb at the BE side in the PCM [13]. The drift of the resistance is accelerated by increasing $|V|$, which is attributed to the increase of local temperature assisting the ionic migration. In fact, as the local temperature in the device increases, the ion migration process is accelerated thanks to the thermal

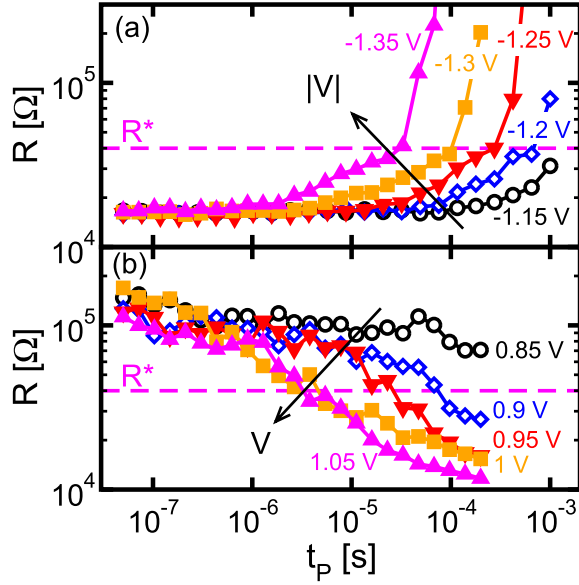Fig. 7. (a) Measured R as a function of pulse duration t_P for a PCM prepared in the full set state for $V < 0$. (b) Measured R for voltage pulses $V > 0$ applied to a state $R = 1.5 \times 10^5$ Ω in (a). Data show a significant voltage acceleration of resistance increase/decrease.
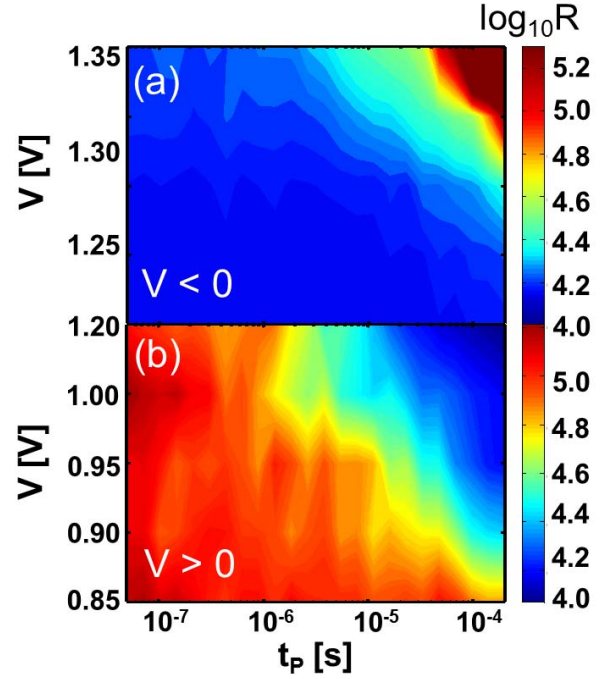

Fig. 8. Measured R (color scale) as a function of t_P and V for ON-state ion-migration experiments similar to Fig. 7 for (a) $V < 0$ and (b) $V > 0$. The change of R shifts to higher V and longer times for negative voltage due to TE.
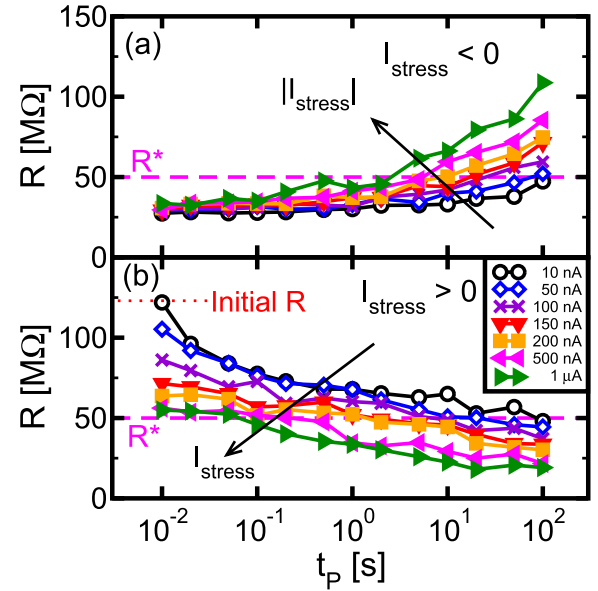

Fig. 9. Measured R as a function of t_P for current stress in the OFF-state at (a) $I_{stress} < 0$ and (b) $I_{stress} > 0$. The positive stress in (b) is applied to the final state obtained after negative stress in (a).

activation of atomic diffusivity [14]. We verified that the process is reversible. Once a resistance $R \approx 10^5$ Ω was reached, the polarity was reversed by applying a voltage pulse below melting with $V > 0$. The positive voltage causes a decrease of resistance, which recovers the original set state, as shown in Fig. 7(b). The decrease of resistance is attributed to the opposite mechanism, where Sb moves toward the BE and Te to the top electrode under the combined effect of Joule heating and electric field [15], [16]. The time needed for ion migration in the ON-state was defined at the crossing with the threshold resistance $R^* = 50$ kΩ. To summarize these results, Fig. 8 shows color maps of R as a function of V (x-axis) and t_P (y-axis) for negative and positive V.

Ion migration was studied in the OFF-state below I_T by applying a constant current $|I_{stress}| \leq 1$ μA to a PCM device in the amorphous phase. The current was kept below 1 μA to avoid threshold switching, and thus ensuring OFF-state conditions in the experiment. The current stress was periodically stopped to perform low-voltage R reading at I_{read}. Fig. 9(a) shows the measured R as a function of the duration t_P of the negative stress. To highlight the change of R under negative stress, we prepared the cell in a positively migrated condition by stressing the cell at 1 μA for 100 s. A current-accelerated increase of resistance, due to ion migration, occurs over a time range $t_P > 10$ ms. Similar to ion migration in the ON-state, the process is accelerated by increasing I_{stress}. The longer time scale for resistance increase with respect to Fig. 7(a) can be ascribed to the lower Joule heating in the OFF-state due to lower current level. To study OFF-state migration at $I_{stress} > 0$, we prepared the cell in a negatively migrated state by 100-s long stress at -1μA. Also, in this case, OFF-state migration is reversible, as shown by the decrease of R in Fig. 9(b). Note that due to TE, even a 10-ms positive stress at $I_{stress} \geq 50$ nA is able to induce significant R change.

The time needed for ion migration in the OFF-state was defined at the crossing with the threshold resistance $R^* = 50$ MΩ. These measurements highlight the relevance of ion migration for read disturb reliability, similar to voltage-accelerated drift and crystallization [10]. Fig. 10 shows color maps of R as a function of I_{stress} (x-axis) and t_P (y-axis) for $I_{stress} < 0$ and $I_{stress} > 0$, confirming the slower ion migration at $V < 0$.
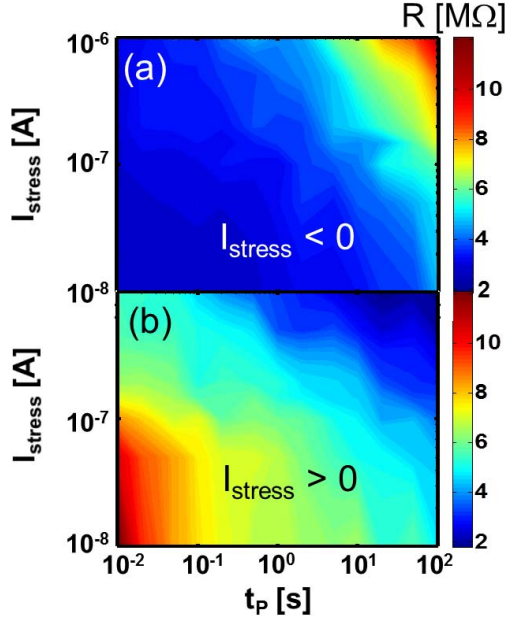
Fig. 10. Measured R as a function of t_P and V for ion-migration experiments in the OFF-state similar to Fig. 9 for (a) $I_{stress} < 0$ and (b) $I_{stress} > 0$.
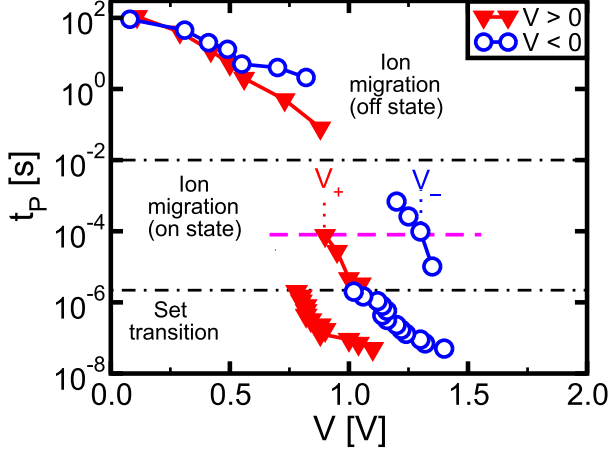

Fig. 11. Measured t_P for ion migration in the ON-state (Fig. 7), ion migration in the OFF-state (Fig. 9), and for set transition [Fig. 3(a)]. The transition time t_P was evaluated at the threshold resistance R^* shown in Figs. 3(a), 7, and 9. The transition voltage at any t_P is systematically higher for $V < 0$, compared with $V > 0$.

V. TE Characteristic

Fig. 11 shows the correlation between pulsewidth t_P and voltage V for set transition (pulse-induced crystallization) and ion migration in either the ON- or OFF-state regime. The reported values for crystallization were obtained by taking the voltage needed for a resistance drop below a threshold $R^* = 1$ MΩ at any given t_P [see Fig. 3(a)]. The values for ion migration were obtained by taking as reference the crossing of $R^* = 50$ kΩ in Fig. 7 for ion migration in the ON-state or $R^* = 50$ MΩ in Fig. 9 for ion migration in the OFF-state. Despite the different ranges of t_P and V, all processes are slower for $V < 0$ due to TE and to the consequent polarity-dependent heating in the GST layer.
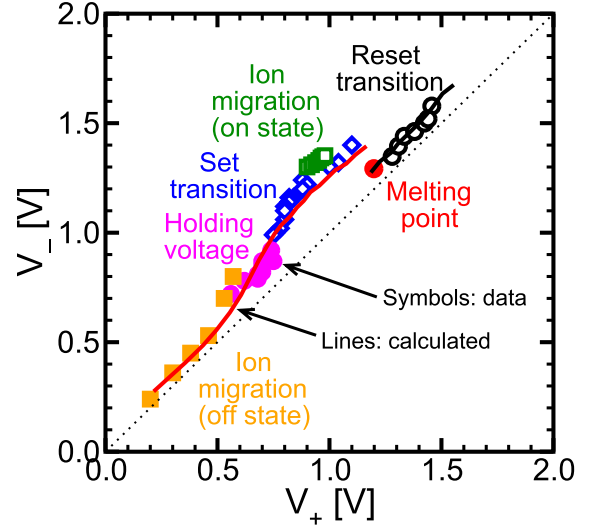

Fig. 12. Correlation plot of measured and calculated characteristic voltages V_+ and V_- for various PCM processes, namely, set transition, reset transition, holding, and ion migration in the ON- and OFF-states. Each pair of voltages V_+ and V_- is identified by a value of t_P in Fig. 11 or by a variable V_{reset} [Fig. 6(b)] or by a threshold resistance R [Fig. 3(b)].

Fig. 12 shows the scatter plot of V_+ and V_-, namely, the voltages needed to accelerate set transition and ion migration at equal t_P in Fig. 11. The figure also includes melting and reset transitions evaluated at increasing threshold resistance from Fig. 3(b) and holding data, namely, V_H at increasing V_{reset} from Fig. 6(b). Irrespective of the specific process considered, all data in Fig. 12 show a universal correlation between V_+ and V_- with $V_- > V_+$ due to the underlying TE. The plot in Fig. 12 shows a simple and effective way to characterize TE in the PCM device.

VI. Modeling and Scaling

TE were modeled by solving carrier and heat conduction equations with Comsol in the cylindrical symmetric 2-D geometry [6], with the boundary conditions in Fig. 1. Thomson and Joule heating were included in the Fourier equation

$$\nabla(k_{th}\nabla T) - J(\nabla\psi + T\nabla S) = 0 \qquad (1)$$

where k_{th} is the thermal conductivity, T is the temperature, ψ is the electrostatic potential, and J is the current density given by

$$J = -\sigma(\nabla\psi + S\nabla T) \qquad (2)$$

where S is the Seebeck coefficient and σ is the electrical conductivity [11]. The model can also describe Peltier heating and cooling at the boundaries of the PCM regions [19]. Fourier equation was solved self-consistently with the current continuity equation

$$\nabla J = 0. \qquad (3)$$

The parameters used in the model at zero electric field and room temperature are shown in Table I. To correctly describe electric and thermal transport in the ON-state, the temperature

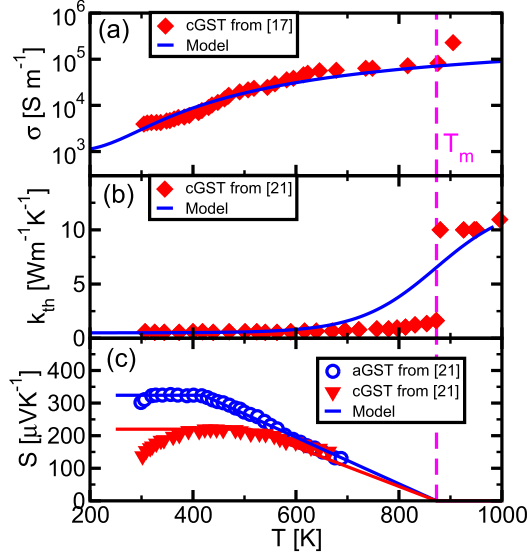| Material	σ [Sm^{-1}]	k_{th} [Wm^{-1}K^{-1}]	S [μVK^{-1}]
cGST	2.8×10^3	0.51	220
aGST	0.8	0.19	320
BE	2.3×10^4	54.5	-10
Top Electrode	2×10^7	174	-1
Insulator	10^{-14}	0.7	0

Fig. 13. (a) Electrical conductivity, (b) thermal conductivity, and (c) Seebeck coefficient, as a function of T for crystalline GST. The Seebeck coefficient for amorphous GST is also shown in (c). Parameters are derived from [17] and [18].
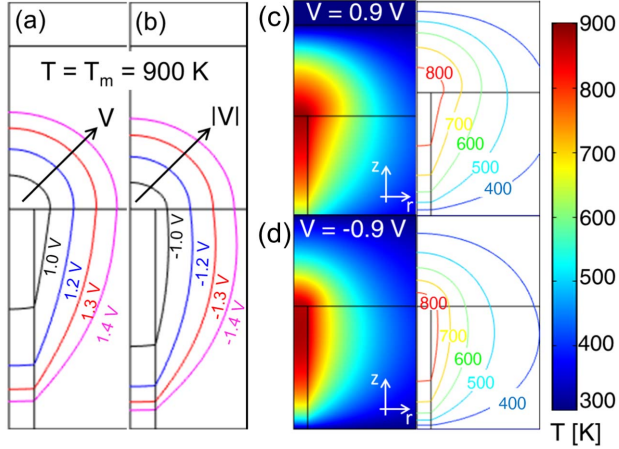

Fig. 14. Calculated contour plots of T_m for increasing voltage at (a) $V > 0$ and (b) $V < 0$. Note the larger molten volume in (a) at the same $|V|$, as a result of Thomson heating in GST. Map of calculated T and contour plot of T for a reset-state PCM during set transition at (c) $V = 0.9$ V and (d) $V = -0.9$ V. The higher heating at $V > 0$ can be attributed to the larger Thomson heat in the GST volume at positive voltage.

dependence of σ, k_{th}, and S was properly considered according to [17], [18], [20], and [21], as shown in Fig. 13.

Fig. 14 shows the calculated contour plot of $T_m = 900$ K for increasing voltages $V > 0$ and $V < 0$ in the set state. The contour shows that the hot spot shifts from the
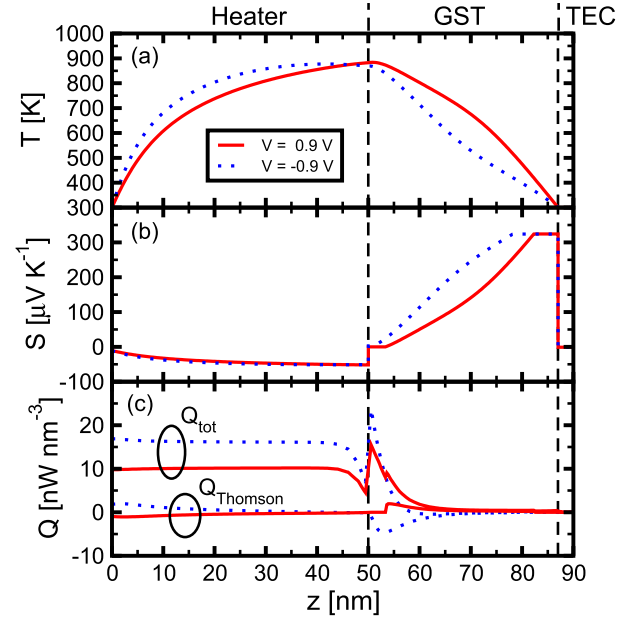

Fig. 15. (a) Calculated profile of T, (b) S, and (c) total/Thomson heat along the symmetry axis (z) during set transition at $V = 0.9$ V [see Fig. 14(c)] and $V = -0.9$ V [see Fig. 14(d)]. The higher heating at $V > 0$ can be attributed to the larger Thomson heat in the GST volume at positive voltage.

chalcogenide volume at $V > 0$ toward the BE for $V < 0$. Fig. 14(c) and (d) shows the contour plot of calculated temperature at $V = 0.9$ and -0.9 V in the reset state during set transition. Heating in GST is clearly more efficient for $V > 0$. To understand the polarity-dependent heating in Fig. 14, Fig. 15 shows the temperature profile along the vertical symmetry axis of the device for positive and negative applied voltage and the corresponding profile of S. The size of ∇S in (1) is the same for positive and negative voltage, while J changes sign thus leading to heating and cooling inside GST for $V > 0$ and $V < 0$, respectively [Fig. 15(c)].

The lower heating efficiency for $V < 0$ explains the origin of $V_- > V_+$ in Fig. 12, which in our model is mainly due to Thomson heating in bulk GST and marginally to Peltier heating at the heater–GST interface. The predominance of Thomson heating in our devices is motivated by the small ΔS between liquid GST and TiN, leading to smaller voltage asymmetry for the points above melting compared with the points below melting in Fig. 12. The calculated positive/negative V to achieve a given T at a fixed z in the amorphous GST volume (related to the choice of R^*) is shown in the correlation plot of Fig. 12. The figure also shows V_+ and V_- for the reset transition in the crystalline phase, obtained as positive/negative voltages leading to the same contour at T_m. The model is able to correctly reproduce the experimental data.

We further used the finite-element model to address the impact of isotropic scaling [22] on TE. Fig. 16 shows the calculated profiles of T and ΔT, namely, the difference between T at $V > 0$ and $V < 0$, for a technology feature size $F = 45$ and 22 nm, at $|V| = 0.9$ V. We defined $\Delta T_{\max}$ as the maximum ΔT inside the GST layer. The model indicates that the same maximum T and ΔT are obtained irrespective of F.

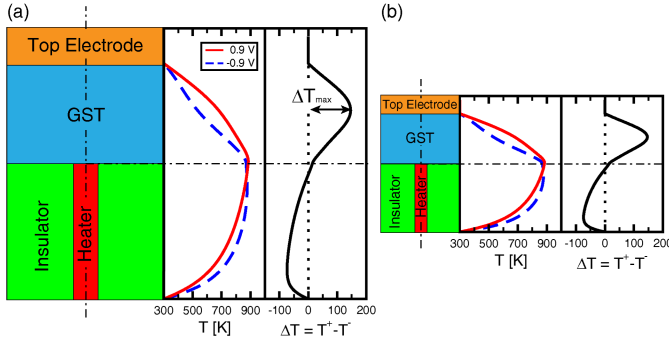Fig. 17 shows a comparison of the calculated universal TE characteristic for $F = 45$ and 22 nm, confirming the

Fig. 16. Profile of calculated T along the vertical (z)-axis at $V = \pm 0.9$ V and the corresponding difference $\Delta T = T_+ - T_-$, for a PCM device in technology nodes (a) $F = 45$ and (b) 22 nm, assuming isotropic downscaling. Note that the same maximum T and maximum temperature difference ΔT_{max} are obtained in the two cases.
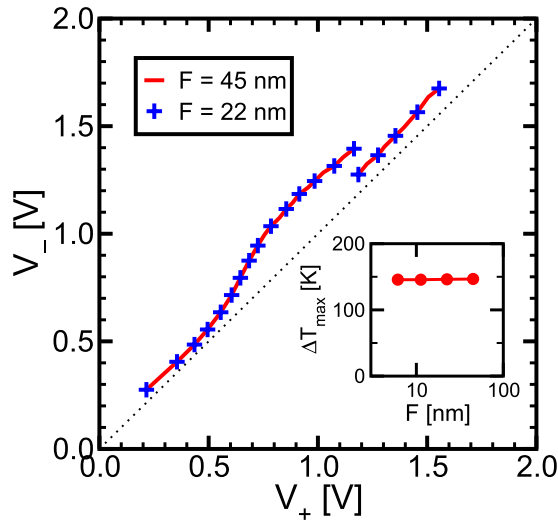

Fig. 17. Correlation of V_+ and V_- for set and reset states of PCM devices of generation $F = 45$ and 22 nm, as shown in Fig. 16. The isotropic scaling leads to the same TE, as confirmed in the inset, showing ΔT_{max} [as shown in Fig. 16(a)] as a function of F.

same impact of TE in the scaled device. The inset shows the calculated ΔT_{max} for four different values of F, namely, $F = 45, 22, 11,$ and 5 nm.

The simulation results confirm that TE do not change as the PCM device is isotropically scaled down, since the predominant Thomson heating is a volume-dependent effect. Note that different results would be obtained if the scaling was not perfectly isotropic, or if the scaling of the device was accompanied by a modification of the process and/or of the materials surrounding the GST layer altering the thermal/electrical boundary resistance and the impact of Peltier heating compared with Thomson heating.

VII. CONCLUSION

We studied the impact of TE in thermally induced PCM processes, such as melting, crystallization, ON/OFF ion migration, and holding. We found that the characteristic voltage V_- for each of the thermally induced phenomena is larger than V_+, namely, $|V_-| > V_+$ due to the polarity-dependent heating caused by TE. A universal characteristic relating V_+ and V_- is

evidenced. TE is reproduced by a model, including Thomson and Peltier effects, able to predict polarity-dependent programming/disturb characteristics at variable PCM size.

REFERENCES

[1] S. Raoux, W. Wełnic, and D. Ielmini, "Phase change materials and their application to nonvolatile memories," *Chem. Rev.*, vol. 110, no. 1, pp. 240–267, 2010.

[2] F. Xiong, A. D. Liao, D. Estrada, and E. Pop, "Low-power switching of phase-change materials with carbon nanotube electrodes," *Science*, vol. 332, no. 6029, pp. 568–570, 2011.

[3] D. Loke *et al.*, "Breaking the speed limits of phase-change memory," *Science*, vol. 336, no. 6088, pp. 1566–1569, Jun. 2012.

[4] M. Rizzi *et al.*, "Reset-induced variability of retention characteristics in phase change memory (PCM)," in *Proc. IRPS*, Jun. 2014, pp. 5E.4.1–5E.4.6.

[5] N. Ciocchini, E. Palumbo, M. Borghi, P. Zuliani, R. Annunziata, and D. Ielmini, "Modeling resistance instabilities of set and reset states in phase change memory with Ge-rich GeSbTe," *IEEE Trans. Electron Devices*, vol. 61, no. 6, pp. 2136–2144, Jun. 2014.

[6] N. Ciocchini, M. Cassinerio, D. Fugazza, and D. Ielmini, "Evidence for non-arrhenius kinetics of crystallization in phase change memory devices," *IEEE Trans. Electron Devices*, vol. 60, no. 11, pp. 3767–3774, Nov. 2013.

[7] G. Servalli, "A 45 nm generation phase change memory technology," in *IEDM Tech. Dig.*, Dec. 2009, pp. 1–4.

[8] D. Ielmini and Y. Zhang, "Evidence for trap-limited transport in the subthreshold conduction regime of chalcogenide glasses," *Appl. Phys. Lett.*, vol. 90, no. 19, p. 192102, 2007.

[9] N. Ciocchini, M. Cassinerio, D. Fugazza, and D. Ielmini, "Modeling of threshold-voltage drift in phase-change memory (PCM) devices," *IEEE Trans. Electron Devices*, vol. 59, no. 11, pp. 3084–3090, Nov. 2012.

[10] N. Ciocchini and D. Ielmini, "Pulse-induced crystallization in phase-change memories under set and disturb conditions," *IEEE Trans. Electron Devices*, vol. 62, no. 3, pp. 847–854, Mar. 2015.

[11] D. T. Castro *et al.*, "Evidence of the thermo-electric Thomson effect and influence on the program conditions and cell optimization in phase-change memory cells," in *IEDM Tech. Dig.*, Dec. 2007, pp. 315–318.

[12] A. Padilla *et al.*, "Voltage polarity effects in Ge$_2$Sb$_2$Te$_5$-based phase change memory devices," *J. Appl. Phys.*, vol. 110, no. 5, p. 054501, 2011.

[13] G. Novielli, A. Ghetti, E. Varesi, A. Mauri, and R. Sacco, "Atomic migration in phase change materials," in *IEDM Tech. Dig.*, Dec. 2013, pp. 22.3.1–22.3.4.

[14] G. C. Sosso, G. Miceli, S. Caravati, F. Giberti, J. Behler, and M. Bernasconi, "Fast crystallization of the phase change compound GeTe by large-scale molecular dynamics simulations," *J. Phys. Chem. Lett.*, vol. 4, no. 24, pp. 4241–4246, 2013.

[15] B. Rajendran *et al.*, "On the dynamic resistance and reliability of phase change memory," in *Symp. VLSI Tech. Dig.*, Jun. 2008, pp. 96–97.

[16] M. H. Lee *et al.*, "The impact of hole-induced electromigration on the cycling endurance of phase change memory," in *IEDM Tech. Dig.*, Dec. 2010, pp. 28.6.1–28.6.4.

[17] A. Cywar, J. Li, C. Lam, and H. Silva, "The impact of heater-recess and load matching in phase change memory mushroom cells," *Nanotechnology*, vol. 23, no. 22, p. 225201, 2012.

[18] N. Kan'an, A. Faraclas, N. Williams, H. Silva, and A. Gokirmak, "Computational analysis of rupture-oxide phase-change memory cells," *IEEE Trans. Electron Devices*, vol. 60, no. 5, pp. 1649–1655, May 2013.

[19] K. L. Grosse, F. Xiong, S. Hong, W. P. King, and E. Pop, "Direct observation of nanometer-scale Joule and Peltier effects in phase change memory devices," *Appl. Phys. Lett.*, vol. 102, no. 19, p. 193503, 2013.

[20] J. Lee, M. Asheghi, and K. E. Goodson, "Impact of thermoelectric phenomena on phase-change memory performance metrics and scaling," *Nanotechnology*, vol. 23, no. 20, p. 205201, May 2012.

[21] A. Faraclas *et al.*, "Modeling of thermoelectric effects in phase change memory cells," *IEEE Trans. Electron Devices*, vol. 61, no. 2, pp. 372–378, Feb. 2014.

[22] U. Russo, D. Ielmini, A. Redaelli, and A. L. Lacaita, "Modeling of programming and read performance in phase-change memories—Part I: Cell optimization and scaling," *IEEE Trans. Electron Devices*, vol. 55, no. 2, pp. 506–514, Feb. 2008.